Configuration Space Representation of MRI Sequences

Carl Ganter

Technical University of Munich, School of Medicine, Department of Diagnostic and Interventional Radiology, Klinikum rechts der Isar der TUM, Munich, Germany

accepted for publication in Magnetic Resonance in Medicine

Category: Full Paper

Word Count (approx.): 3850

Figures: 4

Contact:

Dr. Carl Ganter
Department of Diagnostic and Interventional Radiology
Klinikum rechts der Isar der TUM
Ismaningerstr. 22
81675 Munich
Germany

Email: cganter@tum.de

Abstract

Purpose:

Local solutions provide little intuition about the contrast, generated by MRI sequences with unbalanced gradients. A configuration space representation of the spin density allows to formalize signal localization and thereby overcome these limitations.

Theory and Methods:

The continuous configuration model (CCM) constitutes a Fourier integral decomposition of the spin density, such that intrinsic tissue properties are separated from accumulated effects due to gradients and/or bulk off-resonance. Thereby, any set of local dynamic equations is automatically transformed into a corresponding set of differential equations between configurations.

Results:

The CCM generalizes the Fourier-based EPG formalism such that it becomes applicable to arbitrary MRI sequences. It enables a rigorous and concise treatment of signal localization (selective excitation, spatial encoding), inhomogeneous broadening and motion. Applied to frequency swept NMR, a close connection between SWIFT and SSFP sequences can be found.

Conclusion:

The CCM allows to view arbitrary MRI sequences from a signal processing perspective, which might simplify the development and optimization of novel imaging strategies.

Keywords:

extended phase graphs, EPG, configuration, SWIFT, simulation, signal processing

Introduction

To extract *localized* information via selective excitation and/or spatial encoding, MRI sequences generate spatio-temporally modulated transverse magnetization and reconstruct the recorded signal. In principle, any MRI experiment can be fully described by solving the local dynamic equations. However, the vast majority of MRI sequences comprises *unbalanced* gradients, effecting significant intra-voxel modulations of the magnetization density, which are not related to spatial encoding. For the whole voxel, one therefore has to integrate numerically over many independent local solutions. This is possible, but provides little to no intuition to which extent different magnetization pathways contribute to the reconstructed signal and how the latter precisely depends on tissue properties and sequence design. This deficiency motivated the search for alternative descriptions, which are better adapted to MR imaging.

Already prior to the uprise of MRI, Kaiser et. al. (1) analyzed field gradient effects in NMR Fourier transform spectroscopy by two independent techniques, namely Fourier expansion with respect to local off-resonance and the partition method. Hennig refined the latter by introducing extended phase graphs (EPG) to MRI (2–4). Partition method and EPG are closely related and split the transverse magnetization into two complex conjugate components with opposed phase evolution, as first proposed by Woessner (5). Instantaneous RF pulses effect transitions between these two and the longitudinal component. While the partition method keeps track of each magnetization pathway separately, EPG collects equivalent phase evolutions in *configurations* $F_n^{(*)}$ (transverse components) and Z_n (longitudinal component).

In its original formulation, the EPG framework constitutes a genuine imaging theory of wide scope, applicable to periodic and non-periodic sequences alike. It not only allows to predict the appearance of *echoes*, but also to calculate their amplitudes. Echoes are formally associated with (partial) rephasing of transverse magnetization in a superposition of *isochromats* (= spins with equivalent phase accumulation), while remaining flexible about the physical origin (bulk off-resonance, gradients) of the latter. In the general non-periodic case, echoes can be classified based upon the contributing magnetization pathways (cf. fig. 11 in (6)), but since the number of generated echoes increases rapidly with the number of RF pulses (3), this approach is only practical for a moderate number of RF pulses.

Fortunately, the most prevalent families of MRI sequences comprise free precession intervals of constant duration τ and zero-order gradient moment $\boldsymbol{p}$, such that spins accumulate a constant phase $\vartheta = -\omega\,\tau - \boldsymbol{p}\,\boldsymbol{x}$ in each interval. Although the bulk off-resonance frequency ω can usually be considered as already determined by the position $\boldsymbol{x}$, we will remain flexible and (mostly) treat it as an independent parameter to simplify the discussion of inhomogeneous broadening. In that interpretation, isochromats are defined by the pair $(\boldsymbol{x}, \omega)$. Due to the assumed periodicity, we may write the magnetization density immediately before or after any RF pulse as a Fourier *series* with phase factors $e^{in\vartheta}$ ($n \in \mathbb{Z}$) and the EPG configurations as coefficients. Again, the configuration, which survives the voxel average ($\int d\vartheta \cdots$), defines the EPG echo.

For the remainder of this article, we will restrict our notion of EPG to this periodic, Fourier-based specialization, which has been successfully applied to GRE and (multi-)SE sequences, including effects due to bulk motion (7), isotropic (7) and anisotropic (8) diffusion, magnetization exchange (9) and susceptibility variations (10, 11). An in-depth review of EPG variants has been given by Weigel (6).

The Fourier series representation is particularly valuable, since it isolates spatial modulations due to bulk off-resonance and gradients in the phase factors $e^{in\vartheta}$ and therefore allows for a concise and rigorous treatment of signal localization. In this article, we derive a generalization, which is applicable to arbitrary MRI sequences. In a sloppy notation (the rigorous treatment

follows below), we will switch to an *integral* representation of the isochromat $\boldsymbol{m}\,(\boldsymbol{x},\omega,t)$

$$\sum_{n\in\mathbb{Z}} e^{-\,i\,n\,[\,\omega\,\tau\,+\,\boldsymbol{p}\,\boldsymbol{x}\,]}\,\boldsymbol{m}^{(n)}\,(\boldsymbol{x},t) \quad\longrightarrow\quad \int d\boldsymbol{p}\,d\tau\,e^{-\,i\,[\,\omega\,\tau\,+\,\boldsymbol{p}\,\boldsymbol{x}\,]}\,\hat{\boldsymbol{m}}\,(\boldsymbol{p},\tau,\boldsymbol{x},t) \qquad [1]$$

which we call the *continuous configuration model* (CCM).

The representation becomes unambiguous and meaningful, by demanding that the position dependence of the configurations $\hat{\boldsymbol{m}}\,(\boldsymbol{p},\tau,\boldsymbol{x},t)$ only reflects intrinsic tissue properties, bulk motion and/or $\boldsymbol{B}_1^+$ variations. Just by inserting the CCM into the dynamic equations for the local magnetization density $\boldsymbol{m}\,(\boldsymbol{x},\omega,t)$, we then obtain an equivalent set of partial differential equations for $\hat{\boldsymbol{m}}\,(\boldsymbol{p},\tau,\boldsymbol{x},t)$.

To become more familiar with the CCM, we discuss several examples and topics:

- relation between CCM and EPG
- signal localization in arbitrary MRI sequences
- signal formation in frequency swept NMR (SWIFT) (12)

with additional exemplary material provided in the supporting information (SI), which is available online.

The article finishes with a general discussion how the CCM might benefit the development and optimization of novel imaging sequences.

Theory

Configuration Space Representation

We assume that the state of the local spin density is specified by some vector $\boldsymbol{s}\,(\boldsymbol{x},t)$, such that the magnetization density $\boldsymbol{m}\,(\boldsymbol{x},t)$

$$\boldsymbol{m} \;:=\; \begin{bmatrix} m_x + i\,m_y \\ m_x - i\,m_y \\ m_z \end{bmatrix} \;=:\; \begin{bmatrix} m_+ \\ m_- \\ m_z \end{bmatrix} \qquad [2]$$

can be extracted from the state vector $\boldsymbol{s}$ by a suitable linear operation $\boldsymbol{m} = \boldsymbol{L}\,\boldsymbol{s}$. We further demand that the temporal evolution of the state vector is governed by a differential equation

$$\partial_t\,\boldsymbol{s} \;=\; \boldsymbol{X}\,\boldsymbol{s} \;-\; i\,\big(\,\gamma\,\boldsymbol{G}\,\boldsymbol{x} \;+\; \omega\,\big)\,\boldsymbol{P}\,\boldsymbol{s} \;-\; \boldsymbol{R}\,\big(\,\boldsymbol{s} - \boldsymbol{s}_{eq}\,\big) \qquad [3]$$

$\boldsymbol{G}\,(t)$ denotes the applied gradient and $\omega\,(\boldsymbol{x})$ refers to bulk off-resonance.

As discussed in the introduction, the local state $\boldsymbol{s}\,(\boldsymbol{x},t)$ provides no information about its immediate spatial vicinity. We therefore propose a different representation,

$$\boldsymbol{s}\,(\boldsymbol{x},t) \;=:\; \int d\boldsymbol{p}\,d\tau\,e^{-\,i\,[\,\omega\,(\boldsymbol{x})\,\tau\,+\,\boldsymbol{p}\,\boldsymbol{x}\,]}\,\hat{\boldsymbol{s}}\,(\boldsymbol{p},\tau,\boldsymbol{x},t) \qquad [4]$$

in which spatial modulations due to gradients and bulk off-resonance are expressed by the phase factors $e^{-i\,[\,\omega(\boldsymbol{x})\,\tau\,+\,\boldsymbol{p}\,\boldsymbol{x}\,]}$, while the residual position dependence of $\hat{\boldsymbol{s}}\,(\cdot,\cdot,\boldsymbol{x},\cdot)$ is solely due to intrinsic tissue properties, bulk motion effects or RF pulses. The *configurations* $\hat{\boldsymbol{s}}$ represent the time-dependent state of the local spin ensembles by a vector field in *configuration space* $(\boldsymbol{p},\tau,\boldsymbol{x})$ and we will refer to the representation [4] as *continuous configuration model* (CCM) in the following.

We insert the CCM [4] into the differential equation [3], use partial integration to remove the explicit dependence on $\boldsymbol{x}$, and thereby transform Eq. [3] into

$$\partial_t\,\hat{\boldsymbol{s}}\;=\;\hat{\boldsymbol{X}}\,\hat{\boldsymbol{s}}\;-\;\big(\,\gamma\,\boldsymbol{G}\,\nabla_{\boldsymbol{p}}\;+\;\partial_\tau\,\big)\,\boldsymbol{P}\,\hat{\boldsymbol{s}}\;-\;\boldsymbol{R}\,\big(\,\hat{\boldsymbol{s}}-\hat{\boldsymbol{s}}_{eq}\,\big) \qquad [5]$$

The thermal equilibrium configuration $\hat{\boldsymbol{s}}_{eq}$ contains no history of accumulated phases:

$$\hat{\boldsymbol{s}}_{eq}\big(\boldsymbol{p},\tau,\boldsymbol{x}\big)\;:=\;\delta\,(\boldsymbol{p})\;\delta\,(\tau)\;\boldsymbol{s}_{eq}\,(\boldsymbol{x}) \qquad [6]$$

Technically, we are done with theory.

In the remainder of this article, we will try to justify the more complicated representation [4] of the spin state density.

Methods

Tissue Model

In this article, we consider a pure, static tissue, such that the state vector $\boldsymbol{s}$ can be identified with the magnetization density $\boldsymbol{m}$ and Eq. [3] with the Bloch equations:

- $\boldsymbol{P}=\mathrm{diag}\,[\,1,-1,0\,]$ (precession)
- $\boldsymbol{R}\,(\boldsymbol{x})=\mathrm{diag}\,[\,R_2,R_2,R_1\,]$ (relaxation, repolarization)
- $\boldsymbol{s}_{eq}\,(\boldsymbol{x})=\boldsymbol{m}_{eq}\,(\boldsymbol{x})$ (thermal equilibrium magnetization density)
- $\boldsymbol{X}\,(\boldsymbol{x},t)\equiv\hat{\boldsymbol{X}}\,(\boldsymbol{x},t)=-\,i\,\boldsymbol{\Omega}_1\,(\boldsymbol{x},t)$ (matrix, describing spin rotation by RF pulses)

The interested reader is referred to the (SI) for possible extensions (diffusion, magnetization exchange/transfer, quantum mechanical models), which can be also be described by Eq. [3] but require a different interpretation of (at least some of) its components ($\boldsymbol{s}$, $\boldsymbol{s}_{eq}$, $\boldsymbol{X}$, $\boldsymbol{P}$, $\boldsymbol{R}$).

Including effects due to arbitrary bulk motion is also possible by adding a term on the RHS of Eqs. [3,5]. Again, the details can be found in the (SI).

Numerical Simulations

The numerical implementation of the CCM made use of the hard pulse approximation and allows to include effects due to magnetization exchange/transfer, diffusion and/or bulk motion, as derived in the (SI).

For various examples, we confirm in the supporting information (SI) that the CCM is fully consistent with established theory.

Results

In the following, we first discuss how the CCM generalizes EPG theory, investigate general aspects of signal localization in MRI and then take a closer look at signal formation in frequency swept NMR (SWIFT) (12).

Relation to EPG

Within the *hard pulse approximation* (13) any RF pulse or complete MRI sequence is decomposed into an alternating series of instantaneous small-angle rotations and free precession periods without RF transmission ($\boldsymbol{\Omega}_1 \equiv \mathbf{0}$).

Instantaneous rotations are expressed by linear transformations

$$\hat{\boldsymbol{s}}\left(\boldsymbol{p},\tau,t^{+}\right) \;=\; \boldsymbol{U}\,\hat{\boldsymbol{s}}\left(\boldsymbol{p},\tau,t^{-}\right) \qquad [7]$$

with the rotation matrix $\boldsymbol{U}$ defined precisely as for the state vector $\boldsymbol{s}$.

For any free precession interval $I := [\,t_a, t_b\,]$, the differential equations [5] can be integrated in closed form, but the details depend on the tissue model. Specifically for the Bloch equations (see the (SI) for more examples), we obtain for any $t =: \delta t + t_a \in I$ the following recurrence relations for the transverse and longitudinal components:

$$\hat{m}_{\pm}\left(\boldsymbol{p},\tau,\boldsymbol{x},t\right) \;=\; e^{-\,R_2(\boldsymbol{x})\,\delta t}\,\hat{m}_{\pm}\left(\,\boldsymbol{p}\mp\delta\boldsymbol{p},\tau\mp\delta t,\boldsymbol{x},t_a\right) \qquad [8]$$

$$\hat{m}_{z}\left(\boldsymbol{p},\tau,\boldsymbol{x},t\right) \;=\; e^{-\,R_1(\boldsymbol{x})\,\delta t}\,\hat{m}_{z}\left(\boldsymbol{p},\tau,\boldsymbol{x},t_a\right) \;+\; \left(1-e^{-\,R_1(\boldsymbol{x})\,\delta t}\right)\hat{m}_{eq,z}\left(\boldsymbol{p},\tau,\boldsymbol{x}\right) \qquad [9]$$

The accumulated gradient moment $\delta\boldsymbol{p}\,(t)$ follows the common trajectory:

$$\delta\boldsymbol{p}\,(t) \;:=\; \gamma\int_{t_a}^{t} dt'\,\boldsymbol{G}\left(t'\right) \qquad [10]$$

In the hard pulse approximation, any MRI sequence has a *sparse* support in configuration space, described by a finite set of δ-functions

$$\hat{\boldsymbol{s}}\left(\boldsymbol{p},\tau,\boldsymbol{x},t\right) \;=\; \sum_{n}\delta\left(\boldsymbol{p}\;-\;\boldsymbol{p}_n\left(t\right)\right)\,\delta\left(\tau\;-\;\tau_n\left(t\right)\right)\,\boldsymbol{s}^{(n)}\left(\boldsymbol{x},t\right) \qquad [11]$$

This is so because

- the origin of each magnetization pathway – freshly repolarized longitudinal magnetization in each precession interval – is proportional to $\delta\left(\boldsymbol{p}\right)\delta\left(\tau\right)$, cf. Eq. [6].

- the configurations change their *location* in configuration space during free precession intervals, cf. Eqs. [8,9]. Step size and direction depend on the diagonal elements of $\boldsymbol{P}$, which ultimately increases the number of occupied configurations.
- instantaneous RF pulses [7] *mix* the configuration vector components, but do not affect their location in configuration space.

The representation [11] turns the integral [4] into a (possibly multi-periodic) Fourier *series*.

For *periodic* sequences, the recurrence relations [8,9], reproduce the known EPG expressions (14)

$$\boldsymbol{s}^{(n)} \;=\; \begin{bmatrix} m_{+}^{(n)} \\ m_{-}^{(n)} \\ m_{z}^{(n)} \end{bmatrix} \;=\; \begin{bmatrix} F_n \\ F_{-n}^{*} \\ Z_n \end{bmatrix} \qquad [12]$$

For *non-periodic* sequences, the multi-periodic Fourier representation [4,11], in combination with explicit recurrence relations (such as [8,9]) constitutes a (discrete) extension of the EPG framework.

Signal Localization in MRI

Besides selective excitation, MRI relies on postprocessing of data to generate localized information. The signal $d_\gamma\,(t)$, acquired in coil element γ with sensitivity c_γ, depends on the transverse magnetization density m_+ and noise η_γ

$$d_\gamma\,(t) \;=\; \int d\boldsymbol{x}\, c_\gamma\,(\boldsymbol{x})\; m_+\,(\boldsymbol{x},t) \;+\; \eta_\gamma\,(t) \qquad [13]$$

Because of $m_+ = L_+\,\boldsymbol{s}$, we may apply the CCM [4] and obtain with $\hat{m}_+ := L_+\,\hat{\boldsymbol{s}}$

$$d_\gamma\,(t) \;=\; \int d\boldsymbol{x}\, d\boldsymbol{p}\, d\tau\, e^{-i\,[\,\omega\,(\boldsymbol{x})\,\tau\,+\,\boldsymbol{p}\,\boldsymbol{x}\,]}\, c_\gamma\,(\boldsymbol{x})\; \hat{m}_+\,(\boldsymbol{p},\tau,\boldsymbol{x},t) \;+\; \eta_\gamma\,(t) \qquad [14]$$

(This is the point, where the linearity of $\boldsymbol{L}$ matters, since we pulled L_+ inside the integral on the RHS of Eq. [4].)

From a signal processing perspective, spatial discretization can be viewed as projection to an approximation space (15), spanned by a set of basis functions $\phi_\rho\,(\boldsymbol{x})$. For smooth coil sensitivities c_γ, we then get

$$c_\gamma\,(\boldsymbol{x})\; \hat{m}_+\,(\boldsymbol{p},\tau,\boldsymbol{x},t) \;\approx\; \sum_\rho\, c_{\gamma\rho}\, \hat{m}_{+\rho}\,(\boldsymbol{p},\tau,t)\; \phi_\rho\,(\boldsymbol{x}) \qquad [15]$$

Scaled sinc functions $\phi_\rho\,(\boldsymbol{x}) := \prod_j \,\mathrm{sinc}\,((x_j - x_{\rho j})\,/\Delta x_j)$, located at a regular grid $\boldsymbol{x}_\rho$ of spacing $\Delta\boldsymbol{x}$, constitute the most natural and popular choice for the basis functions ϕ_ρ in MRI. Since their Fourier transform $\phi_\rho\,(\boldsymbol{p}) = e^{-i\,\boldsymbol{p}\,\boldsymbol{x}_\rho}\,\prod_j\,\theta\,(\pi/\Delta x_j - |\,p_j\,|)$ is well localized (θ denotes the Heaviside step function), only configurations $\hat{m}_{+\rho}$ with all $|\,p_j\,| < \pi/\Delta x_j$ (= k-space) contribute to the signal. This is not a stringent criterion though, since the magnetization is usually not

perfectly represented by the basis ϕ_ρ (e.g. due to partial volume effects) and configurations with $|\,p_j\,| > \pi/\Delta x_j$ may leak into the signal.

In summary, the finite set of acquired data $d_{\gamma\kappa} := d_\gamma\,(t_\kappa)$ is approximately linked to the set of discretized configurations $\hat{m}_{+\rho}$ via

$$d_{\gamma\kappa} \;\approx\; \sum_\rho c_{\gamma\rho} \int d\tau\, e^{-i\,\omega_\rho \tau}\, r_\rho\,(\tau) \int_{|\,\boldsymbol{p}\,|<\pi/\Delta\boldsymbol{x}} d\boldsymbol{p}\; e^{-i\,\boldsymbol{p}\,\boldsymbol{x}_\rho}\, \hat{m}_{+\rho}\,(\boldsymbol{p},\tau,t_\kappa) \;+\; \eta_{\gamma\kappa} \qquad [16]$$

The terms in the first integral of Eq. [16] relate to bulk off-resonance and inhomogeneous broadening. $\omega_\rho = \langle\omega\rangle_\rho$ denotes the average bulk resonance frequency over the (voxel) volume, covered by the function $\phi_\rho\,(\boldsymbol{x})$. With respect to susceptibility effects, intra-voxel frequency variations $\omega - \omega_\rho$ are usually treated as independent from gradient-induced modulations and described by a frequency distribution $r_\rho\,(\omega)$. For a (truncated) Lorentzian (16), we obtain the familiar attenuation factor $r_\rho\,(\tau) \approx e^{-\,R'_{2\rho}\,|\tau|}$ for not too small $|\tau|$ (10, 16). (Note that the absolute value is not superfluous, since τ can become negative.)

In Eq. [16] we only cared about the spatial encoding aspect – what about selective excitation? This aspect of localization is also encoded in the $\boldsymbol{p}$-dependence of $\hat{m}_{+\rho}$. For 3D imaging, Eq. [16] still applies and takes care of the shape of the excited block. For 2D imaging, we have to integrate over the slice profile, which can be formally achieved by regarding ϕ_ρ as constant along the slice normal (indicated by '$\perp$'). We then have $\phi_\rho\left(\boldsymbol{p}^{\parallel} + \boldsymbol{p}^{\perp}\right) \propto \delta\left(p^{\perp}\right)$ and it suffices to add a factor $\delta\left(p^{\perp}\right)$ to the integrand in Eq. [16].

Conventional, pulsed FT NMR relies on a *sparse* occupation of k-space, based upon a clear functional separation of (balanced) spatial encoding gradients and unbalanced crushers/spoilers. With respect to the hard pulse approximation [11], this means that all $\boldsymbol{p}_{n_*}\,(t_\kappa)$, which satisfy the condition $|\,\boldsymbol{p}_{n_*}\,(t_\kappa)\,| < \pi/\Delta\boldsymbol{x}$ must have the same value $\boldsymbol{k}_\kappa$. Any other occupied configurations are shifted outside of k-space with crusher gradients or do not exist at all (bSSFP).

For pulsed FT NMR, Eq. [16] therefore simplifies to the more familiar expression

$$d_{\gamma\kappa} \;\approx\; \sum_{\rho,n_*} e^{-i\,\boldsymbol{k}_\kappa \boldsymbol{x}_\rho}\, c_{\gamma\rho}\, e^{-i\,\omega_\rho \tau_{n_*}}\, r_\rho\,(\tau_{n_*})\; \hat{m}^{(n_*)}_{+\rho}\,(t_\kappa) \;+\; \eta_{\gamma\kappa} \qquad [17]$$

where the sum over n_* is restricted to those configurations, which satisfy $\boldsymbol{p}_{n_*}\,(t_\kappa) = \boldsymbol{k}_\kappa$.

Let us finish this section with a few comments:

- The sum over n_* is mainly relevant for bSSFP, since usually only a single n_* is present in sequences with unbalanced gradients.
- The connection between acquired data $d_{\gamma\rho}$ and localized configurations $\hat{m}_\rho$ in Eqs. [16] and [17] is not limited to steady-state conditions, but holds generally and can be used for spatio-temporal reconstructions.
- The functional separation of spatial encoding and crusher gradients is not a mandatory requirement for MRI sequences, as we will see below in our brief discussion of frequency swept NMR (SWIFT) (12). In such cases we have to work with the more general Eq. [16].

Frequency Swept NMR (SWIFT)

While transmit and receive periods are well separated in conventional pulsed FT NMR, a different concept is pursued in SWIFT (12). Here, short signal readouts are interspersed into frequency swept RF pulses in presence of slowly modulated gradients, the latter of which simultaneously encode spatial information and (as we will see) suppress magnetization pathways. As the echo time is essentially zero, SWIFT sequences are predominantly used to visualize tissues with very short T_2 and acquired with rather small (effective) flip angles. Under these conditions, measurable transverse magnetization approximately originates from direct excitation of an essentially time-invariant reservoir of longitudinal magnetization $m_z(\boldsymbol{x})$ (12,17). Within the CCM, this viewpoint corresponds to a linear approximation of the differential equation [5]

$$\partial_t \hat{m}_+ \;\approx\; -\,i\,\Omega_1(t)\;\delta(\boldsymbol{p})\;\delta(\tau)\;m_z(\boldsymbol{x}) \;-\; \big(\,\gamma\,\boldsymbol{G}\,\nabla_{\boldsymbol{p}} \;+\; \partial_\tau \;+\; R_2\,\big)\,\hat{m}_+ \qquad [18]$$

We specified the frequency swept RF pulse by

$$\Omega_1(t) \;:=\; \omega_1(t)\;e^{i\,\varphi(t)} \qquad [19]$$

in the phase-modulated frame, such that ω_1 and φ denote the time-dependent RF amplitude and phase, respectively. The integral of [18] reads

$$\hat{m}_+(\boldsymbol{p},\tau,\boldsymbol{x},t) \;\approx\; -\,i\,\Omega_1(t-\tau)\;\delta(\,\boldsymbol{p}-\tau\,\gamma\,\boldsymbol{G}\,)\;\theta(\tau)\;e^{-\,R_2(\boldsymbol{x})\,\tau}\,m_z(\boldsymbol{x}) \qquad [20]$$

(Interpreted as a distribution (18), the Heaviside step function θ has a derivative: $\theta' = \delta$)

After inserting this solution into the CCM [4], the acquired signal [13] can be written as a convolution

$$d(t) \;\approx\; h * \Omega_1(t) \qquad [21]$$

of the impulse response function (= FID)

$$h(t) \;:=\; -\,i\,\theta(t)\int d\boldsymbol{x}\,e^{-\,i\,[\,\omega(\boldsymbol{x})\,+\,\gamma\,\boldsymbol{G}\,\boldsymbol{x}\,]\,t}\,e^{-\,R_2(\boldsymbol{x})\,t}\,m_z(\boldsymbol{x}) \qquad [22]$$

and the RF pulse $\Omega_1(t)$. In the original SWIFT article (12), essentially the same convolution formula (Eq. 4 therein) was motivated with ideas from stochastic NMR (19,20).

Since the signal purely relies on the recovery of longitudinal magnetization, it depends on T_1 only and may be expressed by an Ernst formula (12). On the other hand, the bright CSF in fig. 7 of ref. (21) indicates that transverse coherences should be taken into account for $T_2 > \mathrm{TR}$ and moderate flip angles.

In order to take a closer look at signal formation, let us consider a sequence of frequency swept RF pulses of duration $T_p = \mathrm{TR}$ in presence of a *constant* gradient $\boldsymbol{G}$, as depicted in Fig. 1. The magnetization density at the local resonance frequency $\widetilde{\omega} := \omega + \gamma\, \boldsymbol{G}\, \boldsymbol{x}$ approaches a TR-periodic steady-state

$$m_+ (\widetilde{\omega}, \boldsymbol{x}, t) \;=:\; \sum_j e^{-\,ij\,2\pi\,t/\mathrm{TR}}\, f_j (\widetilde{\omega}, \boldsymbol{x}) \qquad [23]$$

In the rapid passage linear region, excitations occur approximately instantaneously at those time points $t(\widetilde{\omega})$, when the swept RF frequency ω_{RF} matches the local resonance frequency $\widetilde{\omega}$ (22,23). In this simplified view, the local steady-state allows for a conventional EPG decomposition in terms of bSSFP configurations $m_+^{(n)}(\boldsymbol{x})$ (10), leading to a closed form estimate of the Fourier coefficients f_j:

$$\begin{aligned} f_j (\widetilde{\omega}, \boldsymbol{x}) \;&\approx\; \frac{w(\widetilde{\omega})}{\mathrm{TR}} \cdot \int_0^{\mathrm{TR}} dt'\, e^{ij\,2\pi\,(t' + t(\widetilde{\omega}))/\mathrm{TR}}\, e^{-\,[\,i\,\widetilde{\omega} + R_2(\boldsymbol{x})\,]\,t'} \sum_{n\in\mathbb{Z}} e^{-\,i\,\widetilde{\omega}\,n\,\mathrm{TR}}\, m_+^{(n)}(\boldsymbol{x}) \qquad [24] \\ &=\; \frac{w(\widetilde{\omega})}{\mathrm{TR}}\, e^{ij\,2\pi\,t(\widetilde{\omega})/\mathrm{TR}} \cdot \frac{1 - e^{-\,[\,i\,\widetilde{\omega} + R_2(\boldsymbol{x})\,]\,\mathrm{TR}}}{i\,\widetilde{\omega} \;-\; [\,ij\,2\pi/\mathrm{TR} - \;R_2(\boldsymbol{x})\,]} \cdot \sum_{n\in\mathbb{Z}} e^{-\,i\,\widetilde{\omega}\,n\,\mathrm{TR}}\, m_+^{(n)}(\boldsymbol{x}) \end{aligned}$$

The window function $w(\widetilde{\omega}) \approx \theta(\Omega - |\,\widetilde{\omega}\,|)$ reflects the finite bandwidth of the frequency sweep.

For a constant gradient $\boldsymbol{G}$, a configuration space representation [4], which satisfies the differential equation [5] in the free precession periods between the instantaneous RF pulses, is given by

$$\hat{m}_+ (\boldsymbol{p}, \tau, \boldsymbol{x}, t) \;\approx\; \delta(\,\boldsymbol{p} - \tau\gamma\,\boldsymbol{G}\,) \cdot \int \frac{d\widetilde{\omega}}{2\pi}\, e^{i\,\widetilde{\omega}\,\tau}\, m_+ (\widetilde{\omega}, \boldsymbol{x}, t) \qquad [25]$$

In the bSSFP approximation [24], the integral in Eq. [25] turns into a contour integral along the imaginary axis after variable substitution $z := i\,\widetilde{\omega}$. To estimate its value, we make use of the residue theorem, noting that the analytic continuation $\hat{f}_j(z, \boldsymbol{x}) := f_j(\widetilde{\omega}, \boldsymbol{x})$ exhibits singularities at $z_j := ij\,2\pi/\mathrm{TR} - R_2(\boldsymbol{x})$. The behavior at large $|\,z\,|$ is dominated by exponentials of the form $e^{z\,\tau_*}$ and, as usual, we close the integration contour to the side where they become small, as shown in Fig. 2. Since $\mathrm{Re}(z_j) < 0$, this implies that the poles are only enclosed for $\tau_* > 0$

$$\begin{aligned} \hat{m}_+ (\boldsymbol{p}, \tau, \boldsymbol{x}, t) \;&\approx\; \delta(\,\boldsymbol{p} - \tau\gamma\,\boldsymbol{G}\,) \cdot \frac{1}{\mathrm{TR}} \sum_{\substack{j,n \\ |\,\mathrm{Im}(z_j)\,| < \Omega}} e^{ij\,2\pi\,\left(\tau - t + \hat{t}(z_j)\right)/\mathrm{TR}}\, e^{-\,R_2(\boldsymbol{x})\,(\tau - n\,\mathrm{TR})} \\ &\cdot\, [\,\theta(\tau \;-\; n\,\mathrm{TR}) \;-\; \theta(\tau \;-\; (n+1)\;\mathrm{TR})\,]\; m_+^{(n)}(\boldsymbol{x}) \qquad [26] \end{aligned}$$

as expressed by the θ-functions. We further assumed that the chosen window function w permits an analytical continuation $\hat{w}$ with $\hat{w}(z_j) \approx w(j\,2\pi/\mathrm{TR})$, such that the summation is approximately restricted to $|\,\mathrm{Im}(z_j)\,| \;<\; \Omega$.

For $T_2 \gg \mathrm{TR}$, moderate flip angles and sufficient distance from $t = t(\widetilde{\omega})$, the bSSFP picture approximates the local magnetization density m_+ and the configuration $\hat{m}_+$ reasonably well, cf. Fig. 3.

Since only configurations with $|\, p_j \,| < \pi/\Delta x_j$ (in all directions j) contribute to the reconstructed localized signal, only two configurations from Eq. [26] are observable in each acquired spoke, if the gradient amplitude is adapted to the desired resolution ($G = 2\pi/\gamma\,\mathrm{TR}\,\Delta x$):

- *Prior* to the effective excitation time $t\,(\widetilde{\omega})$, we observe an ECHO ($n = -1$) moving *towards* the center at $\boldsymbol{p} = \boldsymbol{0}$.
- *After* the effective excitation time $t\,(\widetilde{\omega})$, we observe a FID ($n = 0$) moving *away* from the center.

Fig. 4 shows how the configurations spread in configuration space as a function of time. To compare with the sparse k-space occupation in pulsed FT NMR, we also include a corresponding plot for the DESS (24) sequence, depicted in Fig. 1. The script `swift.m`, which was used to generate Figs. 3 and 4, also illustrates the sudden transition from the ECHO to the FID signal around the k-space center.

In a real SWIFT acquisition, the gradient $\boldsymbol{G}$ must be reoriented from pulse to pulse in order to allow for a 3D reconstruction. This can also be simulated with `swift.m` (consistent with our choice $T_p = \mathrm{TR}$, under the assumption of a constant rotation speed) and we observe a signal decay, increasing with speed of rotation and distance from the isocenter. It is therefore important to ensure a sufficiently adiabatic reorientation of $\boldsymbol{G}$.

In summary, with respect to signal formation, SWIFT and SSFP are strongly connected, in accordance with the observed similar contrast. The main difference lies in the spatial encoding, as visualized in Fig. 4 b (SWIFT) versus Fig. 4 c (DESS). In DESS, reconstruction of FID and ECHO poses no problems, since both signals are well separated from each other and from the RF pulses. In contrast, the transition ECHO → FID in SWIFT conincides with effective excitation near the center of k-space. Together with the superposition of different k-space locations in the recorded data, spatial reconstruction becomes more challenging (cf. Discussion).

Discussion

In this article, we proposed the continuous configuration model (CCM) [4] as a representation of the magnetization density, devised to simplify the handling of signal localization in arbitrary MRI sequences. Just by inserting the CCM into any appropriate set of dynamic equations [3], governing the state vector $\boldsymbol{s}$ of the spin density, we obtained a related set of differential equations [5] for the configurations $\hat{\boldsymbol{s}}$. It was shown that the data $d_{\gamma\kappa}$, acquired in any MRI sequence, are directly linked to the discretized configurations $\hat{m}_{+\rho} = L_+\,\hat{\boldsymbol{s}}_\rho$ via Eq. [16].

We convinced ourselves that the CCM generalizes the extended phase graph (EPG) formalism, in particular its most commonly encountered Fourier-based variant for periodic sequences. While the Fourier integral definition of EPG states (6) can be considered as applicable to arbitrary MRI sequences, the CCM shows how to update them without having to resort to local solutions.

The CCM isolates spatial modulations due to gradients and bulk off-resonance in the phase factors $e^{-i\,[\,\omega(\boldsymbol{x})\,\tau\,+\,\boldsymbol{p}\,\boldsymbol{x}\,]}$. Precisely as in EPG, the Fourier variables $(\boldsymbol{p}, \tau)$ characterize the magnetization pathways, which contribute to a given configuration:

- $\boldsymbol{p}$ = accumulated net gradient moment
- τ = accumulated net precession time

The configuration $\hat{\boldsymbol{s}}\,(\boldsymbol{p}, \cdot, \cdot, \cdot)$ therefore determines the

- shape of the selectively excited slice/volume
- spatial encoding for $|\,p_j\,| < \pi/\Delta x_j$ (k-space)
- suppression of magnetization pathways for $|\,p_j\,| > \pi/\Delta x_j$ (crushers)

On the other hand, $\hat{\boldsymbol{s}}\,(\cdot, \tau, \cdot, \cdot)$ controls

- the local signal phase (voxel average)
- signal loss due to inhomogeneous broadening (susceptibility effects)

Finally, the spatial dependence $\hat{\boldsymbol{s}}\,(\cdot, \cdot, \boldsymbol{x}, \cdot)$ is relevant for discretization and relates to

- local tissue properties
- bulk motion
- $\boldsymbol{B}_1^+$ inhomogeneity

With respect to gradients, pulsed FT NMR sequences share a clear functional separation between localization and contrast generation (cf. Eq. [17]) and this is the reason, why spatial encoding gradients can usually be ignored in simulations. The EPG framework has been successfully applied to virtually any relevant pulsed FT NMR sequence, up to randomized variants like unbalanced magnetic resonance fingerprinting (MRF) (25). Additional value, generated by the flexibility of the CCM, should therefore mainly be expected in the assessment of experimental imperfections, e.g. due to

- variable eddy currents (e.g. caused by rotating spirals in MRF)
- the leakage of unwanted magnetization pathways into the reconstructed signal.

To demonstrate that the CCM is not limited to pulsed FT NMR sequences, we took a closer look at frequency swept NMR. SWIFT (12) is predominantly recognized as a silent zero echo time sequence, but the analysis of signal formation revealed a close connection to unbalanced SSFP and a related contrast, which can be expected to persist under more general conditions such as variable flip angles and/or phase cycling. Beyond its current applications, SWIFT could therefore become of interest for silent conventional or quantitative MRI.

Image reconstruction is more involved though, since the acquired data $d_{\gamma\kappa}$ no longer correspond to well-defined locations in k-space (compare Figs. 4 b and c). Since each gradient serves more than one purpose in frequency swept NMR, we further need to disentangle tissue properties from spatial encoding in the function $\hat{m}_{+\rho}\,(\boldsymbol{p}, \cdot, \cdot)$ in Eq. [16]. We actually did so in the bSSFP approximation [26], when we attributed the observed contrast of SWIFT to the SSFP configurations $\hat{m}_{+\rho}^{(0)}$ (FID) and $\hat{m}_{+\rho}^{(-1)}$ (ECHO). But to construct a proper encoding matrix, Eq. [26] does not suffice as an input to Eq. [16], because of the oversimplistic assumption of instantaneous excitation at $t = t_{\widetilde{\omega}}$ (cf. Fig. 3 c). Since the latter conincides with the transition ECHO $\rightarrow$ FID at $\boldsymbol{p} = \boldsymbol{0}$, the most pivotal region for spatial encoding, the detailed properties of the RF pulse need to be taken into account, as done in the convolution method (12) or the more k-space oriented algebraic approach (17). A detailed analysis of the options to improve existing reconstructions along these lines is beyond the scope of this article though.

In summary, the CCM constitutes a generalization of the EPG framework, applicable to arbitrary MRI sequences and tissues, in which the differential equations [5] describe the transport, modulation, relaxation and recreation of signal 'energy'. Signal localization is treated as an inverse problem, with data consistency defined by Eq. [16]. This signal processing perspec-

tive could be advantageous to explore the available options for encoding and reconstructing diagnostic information with MRI.

Data Availability Statement

To support reproducible research, the MATLAB code (R2020b, Natick, Massachusetts: The MathWorks Inc.), together with all scripts, used to produce the figures of this manuscript and the (SI), is freely available (26). (The corresponding script names are given in the figure captions.) Actual versions of the software can be obtained at https://github.com/cganter/CoMoTk.

Acknowledgements

The author thanks Marco Hauke and Dominik Weidlich from the BMRR group (https://bmrrgroup.de) for extensive tests of the simulation software.

References

1. Kaiser R, Bartholdi E, Ernst RR. Diffusion and field-gradient effects in NMR Fourier spectroscopy. The Journal of Chemical Physics 1974;60:2966–2979. doi:10.1063/1.1681477.
2. Hennig J. Multiecho imaging sequences with low refocusing flip angles. Journal of Magnetic Resonance (1969) 1988;78:397–407. doi:10.1016/0022-2364(88)90128-x.
3. Hennig J. Echoes—how to generate, recognize, use or avoid them in MR-imaging sequences. part I: Fundamental and not so fundamental properties of spin echoes. Concepts Magn Reson 1991;3:125–143. doi:10.1002/cmr.1820030302.
4. Hennig J. Echoes—how to generate, recognize, use or avoid them in MR-imaging sequences. part II: Echoes in imaging sequences. Concepts Magn Reson 1991;3:179–192. doi:10.1002/cmr.1820030402.
5. Woessner DE. Effects of diffusion in nuclear magnetic resonance spin-echo experiments. The Journal of Chemical Physics 1961;34:2057–2061. doi:10.1063/1.1731821.
6. Weigel M. Extended phase graphs: Dephasing, RF pulses, and echoes - pure and simple. J Magn Reson Imaging 2014;41:266–295. doi:10.1002/jmri.24619.
7. Sodickson A. A generalized k-space formalism for treating the spatial aspects of a variety of NMR experiments. Prog Nucl Magn Reson Spectrosc 1998;33:77–108. doi:10.1016/s0079-6565(98)00021-1.
8. Weigel M, Schwenk S, Kiselev V, Scheffler K, Hennig J. Extended phase graphs with anisotropic diffusion. J Magn Reson 2010;205:276–285. doi:10.1016/j.jmr.2010.05.011.
9. Malik SJ, Teixeira RPA, Hajnal JV. Extended phase graph formalism for systems with magnetization transfer and exchange. Magn Reson Med 2017;80:767–779. doi:10.1002/mrm.27040.
10. Ganter C. Static susceptibility effects in balanced SSFP sequences. Magn Reson Med 2006;56:687–691. doi:10.1002/mrm.20986.

11. Leupold J. Steady-state free precession signals of arbitrary dephasing order and their sensitivity to T2*. Concepts in Magnetic Resonance Part A 2017;p. e21435.

12. Idiyatullin D, Corum C, Park JY, Garwood M. Fast and quiet MRI using a swept radiofrequency. Journal of Magnetic Resonance 2006;pp. 342–349. doi:10.1016/j.jmr.2006.05.014.

13. Subramanian VH, Eleff SM, Rehn S, Leigh JS. An exact synthesis procedure for frequency selective pulses. Proc Int Soc Magn Reson Med 1986;5:1452.

14. Scheffler K. A pictorial description of steady-states in rapid magnetic resonance imaging. Concepts Magn Reson 1999;11:291–304.

15. Mallat S, Peyré G. A Wavelet Tour of Signal Processing. Elsevier, 1999. ISBN 9780124666061. doi:10.1016/b978-0-12-466606-1.x5000-4.

16. Yablonskiy DA, Haacke EM. Theory of NMR signal behavior in magnetically inhomogeneous tissues: The static dephasing regime. Magnetic Resonance in Medicine 1994;pp. 749–763. doi:10.1002/mrm.1910320610.

17. Weiger M, Hennel F, Pruessmann KP. Sweep MRI with algebraic reconstruction. Magnetic Resonance in Medicine 2010;pp. 1685–1695. doi:10.1002/mrm.22516.

18. Lighthill MJ. Introduction to Fourier Analysis and Generalised Functions. Cambridge University Press, 1958. ISBN 9781139171427. doi:10.1017/cbo9781139171427.

19. Ernst RR. Magnetic resonance with stochastic excitation. Journal of Magnetic Resonance (1969) 1970;pp. 10–27. doi:10.1016/0022-2364(70)90004-1.

20. Kaiser R. Coherent spectrometry with noise signals. Journal of Magnetic Resonance (1969) 1970;pp. 28–43. doi:10.1016/0022-2364(70)90005-3.

21. Idiyatullin D, Corum C, Moeller S, Garwood M. Gapped pulses for frequency-swept MRI. Journal of Magnetic Resonance 2008;pp. 267–273. doi:10.1016/j.jmr.2008.05.009.

22. Pipe JG. Spatial encoding and reconstruction in MRI with quadratic phase profiles. Magnetic Resonance in Medicine 1995;pp. 24–33. doi:10.1002/mrm.1910330105.

23. Park JY, Delabarre L, Garwood M. Improved gradient-echo 3D magnetic resonance imaging using pseudo-echoes created by frequency-swept pulses. Magnetic Resonance in Medicine 2006;pp. 848–857. doi:10.1002/mrm.20821.

24. Bruder H, Fischer H, Graumann R, Deimling M. A new steady-state imaging sequence for simultaneous acquisition of two MR images with clearly different contrasts. Magnetic Resonance in Medicine 1988;pp. 35–42. doi:10.1002/mrm.1910070105.

25. Jiang Y, Ma D, Seiberlich N, Gulani V, Griswold MA. MR fingerprinting using fast imaging with steady state precession (FISP) with spiral readout. Magnetic Resonance in Medicine 2015;pp. 1621–1631. doi:10.1002/mrm.25559.

26. Ganter C. Configuration Model Toolkit (CoMoTk) 2021;doi:10.5281/zenodo.5347194.

Figures

Figure 1

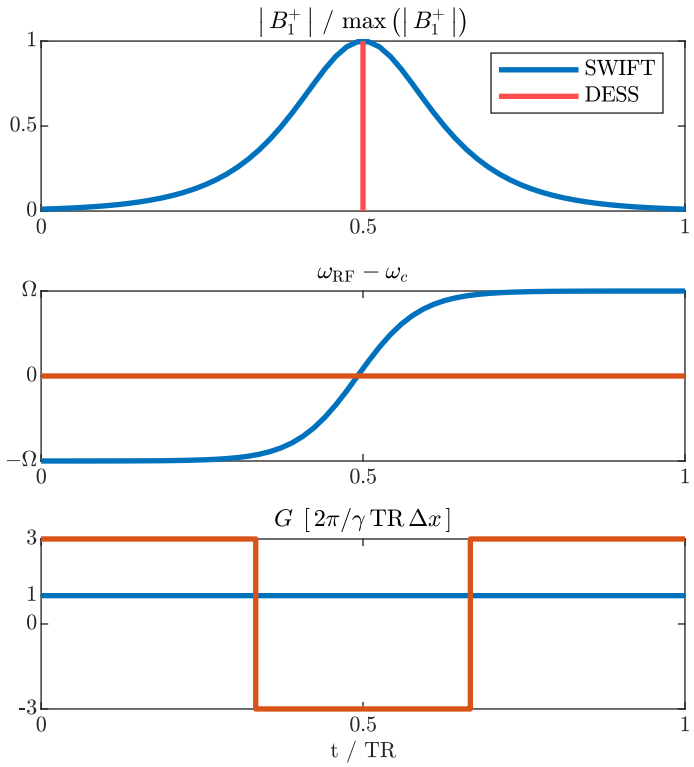

Figure 1: The steady-state of SWIFT (12) is simulated for a frequency swept hyperbolic secant (HS1) pulse of duration $T_p = \mathrm{TR}$ in presence of a constant gradient $\boldsymbol{G}$ (blue). To visualize the different occupation of configuration space in pulsed FT NMR, we also simulate a double echo steady-state (DESS) (24) sequence (red), with an instantaneous RF pulse located at TR/2. For a meaningful comparison with SWIFT, the full readout gradient (spatial encoding and crusher) is shown.

Figure 2

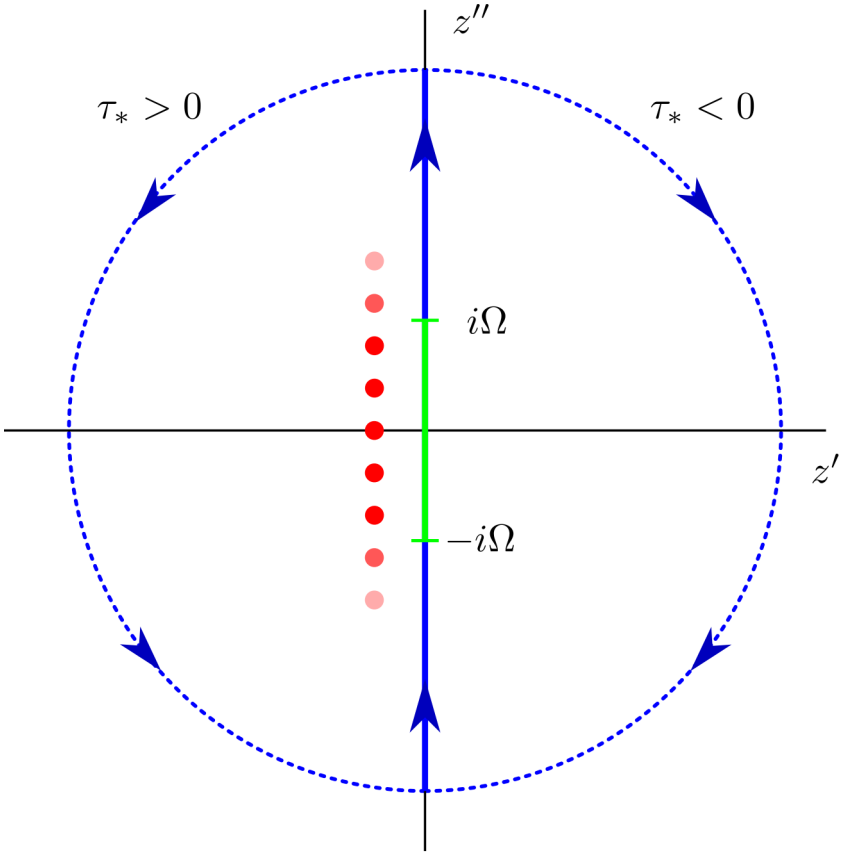

Figure 2: The integration contour ($z := z' + iz''$) to estimate the integral [25]. As explained in the text, the sign of τ_* determines, whether the singularities z_j are included or not. The green range on the imaginary axis correponds to the bandwidth of the RF frequency sweep. We assume that the analytical continuation of the window function $w(\widetilde{\omega})$ in Eq. [24] restricts the relevant residues essentially to this range (as indicated by the shaded red circles).

Figure 3

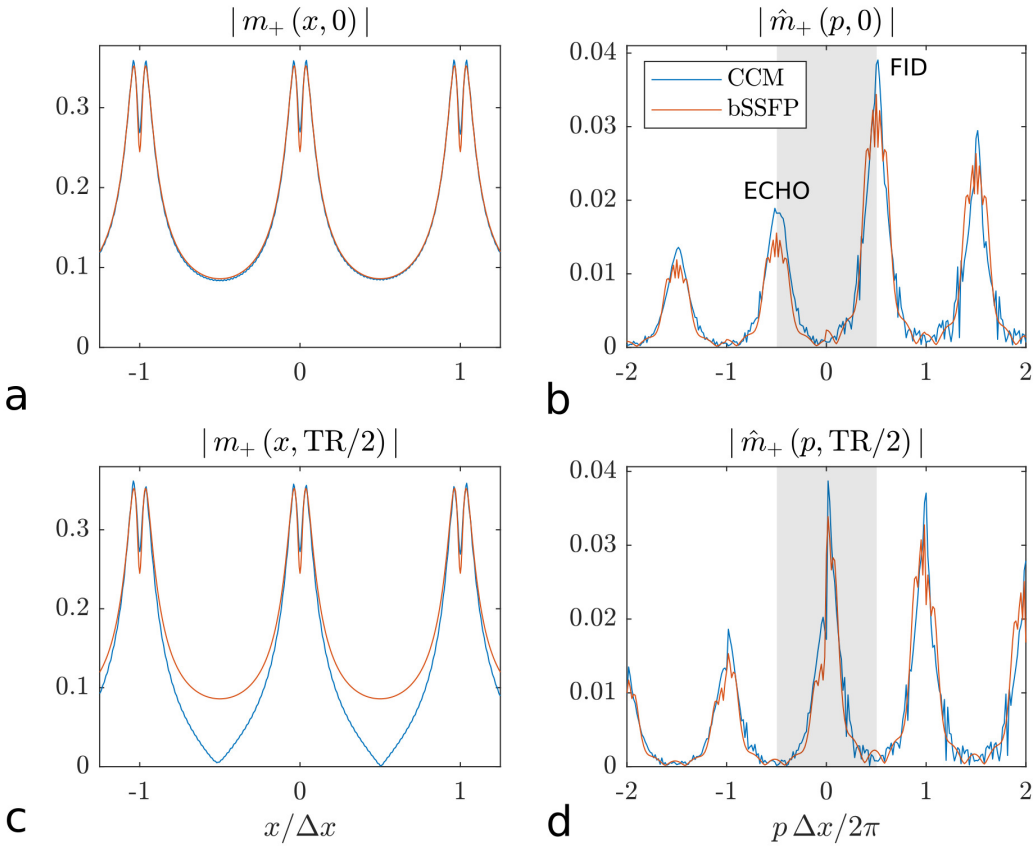

Figure 3: SWIFT: CCM (blue) compared with bSSFP approximation (red). The simulation was conducted for a gapped hyperbolic secant (HS1) RF pulse with 60 segments, full duty cycle, $T_p = \mathrm{TR} = 1\,\mathrm{ms}$, effective flip angle $\alpha = 10°$ and 100 kHz bandwidth. The gradient $\boldsymbol{G}$ was kept constant in order to generate a steady-state. Its magnitude satisfied $\gamma\, G\, \mathrm{TR}\, \Delta x = 2\pi$, compatible with a resolution of $\Delta x = 1\,\mathrm{mm}$. A pure on-resonant ($\omega = 0$) tissue was assumed with $T_1/T_2 = 20/10\,\mathrm{ms}$. The simulation shows the intra-voxel profile $|\,m_+\,(x,t)\,|$ (**a**,**c**) and the configuration $|\,\hat{m}_+\,(p,t)\,|$ (**b**,**d**). The grey shaded area corresponds to the reconstructible range $|\,p\,| < \pi/\Delta x$ (= conventional k-space). For $t = 0$ (**a**,**b**), i.e. with maximal (average) temporal separation from the effective excitation, a reasonable agreement between the full CCM simulation and the bSSFP approximations [23,24] and [26] is obtained. This is just the time, when the FID ($n = 0$) and ECHO ($n = -1$) peaks are located in the outer parts of k-space. The limitations of the instantaneous excitation picture become apparent close to $t = t_{\widetilde{\omega}} \approx \mathrm{TR}/2$ (**c**,**d**), particularly in the steady-state profile (**c**). Note how the identity of the configuration peaks changes at those locations, where p is some integer multiple of $2\pi/\Delta x$ (**d**). (The provided MATLAB script `swift.m` shows the evolution during the whole interval $0 < t < \mathrm{TR}$ in more detail.)

Figure 4

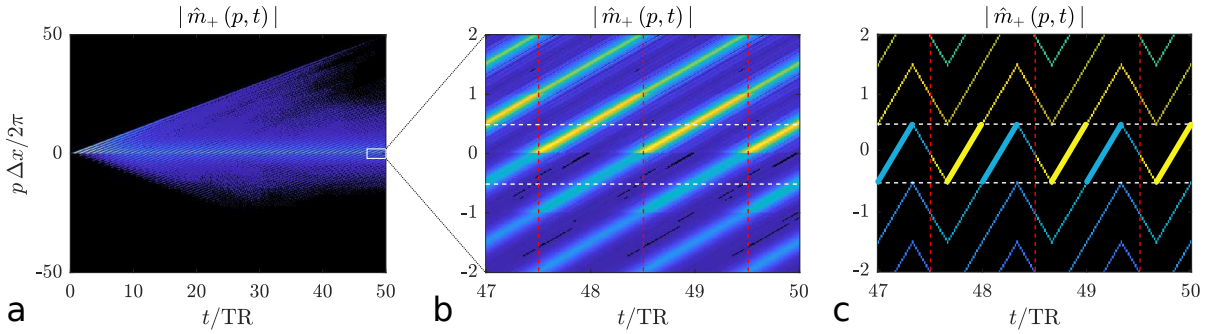

Figure 4: (**a**) Configuration space occupation as a function of time for the simulation shown in Fig. 3 with selected detail (**b**). For comparison, we show the corresponding detail for the DESS sequence from Fig. 1 in (**c**). The vertical dashed red lines in (**b**,**c**) indicate the center of the HS1 pulse (SWIFT) and the location of the instantaneous RF pulse (DESS), respectively. The horizontal dashed white lines mark the bounds of k-space and only the enclosed region is usable for reconstruction. For DESS, the thick lines accentuate the readout periods for the FID (yellow) and ECHO (blue). Different from SWIFT, only a single configuration is acquired at any time point.

Configuration Space Representation of MRI Sequences Supporting Information

Carl Ganter

Contents

1 Consistency Checks and Simple Examples

The following material illustrates that the continuous configuration model (CCM) complies with established theory (Bloch simulations, EPG) and discusses a few simple examples. All calculations were performed with the freely available configuration model toolkit (CoMoTk) (1). The script names can be found in the figure captions.

Equations from the main text are referenced by numbers only (like [1] instead of [S1]).

1.1 Comparison with Bloch Simulation

Sequence design usually starts with a simplified viewpoint, neglecting the finite duration of transmit/receive periods or imperfect slice profiles. In this picture, only unbalanced gradients are taken into account, which may either allow for rephasing of transverse magnetization (crushers) or not (spoilers). According to Eq. [17], the reconstructed signal of conventional MRI sequences is then determined by discrete configurations $\hat{m}^{(n)}_{+\rho}$, regardless of whether the sequence is balanced or unbalanced[1].

Results for a randomized balanced SSFP sequence are displayed in Figure S1, with relevant parameter settings given in the caption. As expected and required, CCM agrees with Bloch simulation. To reduce computation time and avoid potential memory overflow in the CCM simulation, small configurations were discarded after each time interval.

1.2 (multi-)SE, SSFP and Extended Phase Graphs (EPG)

(multi-)SE sequences comprise a series of free precession periods of constant duration $\tilde{\tau}$ (= half time to first echo) and zero-order gradient moment $\tilde{\boldsymbol{p}}$ (due to crushers), separated by RF pulses or signal readouts. The equivalence [12] between CCM and EPG[2] is verified in Figure S2 (left).

Similar to spin echoes, balanced SSFP (bSSFP) sequences show rephasing effects at TE $\approx$ TR/2 (4), as long as the variation of the (static) resonance frequency does not become too large (2). Figure S2 (right) shows that this effect can be accurately described in the CCM and also agrees with EPG (3).

1.3 Amplitude Modulated RF Pulses

Figure S3 compares a Sinc-shaped RF pulse in hard pulse approximation (parameters in the figure caption), acting on longitudinal proton density with $m_{eq} = 1$. For the CCM, a pure tissue was assumed with $R_1 = 0$, $R_2 = 0.1$ ms^{-1} in absence of diffusion ($D = 0$). The observed difference between CCM and SLR design (5) is caused by transverse relaxation and vanishes for $R_2 \to 0$, as required.

1.4 Frequency Modulated RF Pulses

Figure S4 shows[3] the rapid adiabatic full-passage (AFP) for an hyperbolic secant (HS1) pulse in comparison with a chirp pulse, with parameters taken from Table 1 in (6). Again, effects due to intrinsic tissue properties are automatically included in the CCM. As an example, Figure S4 also demonstrates incomplete refocusing, when T_2 becomes comparable to the pulse duration.

[1] In pulsed FT NMR, we always assume crushers to be strong enough to shift unwanted magnetization pathways outside of the imaging region (= k-space, defined by $|\boldsymbol{p}| < \pi/\Delta\boldsymbol{x}$).

[2] Where the spin echo is associated with the index $n = 0$ because of the in-plane crushers.

[3] Frequency and phase modulation may be regarded as equivalent (6). The latter was chosen (the CCM can handle both cases) for the simulation.

1.5 Realistic Sequences

Figure S5 shows how the transient phase of a conventional bSSFP sequence depends on the RF pulse shape. The frequency of the transient oscillations apparently decreases with the quality of the slice profile. (For B_1^+ maps, derived from this oscillation frequency (7), this effect is of quantitative relevance.)

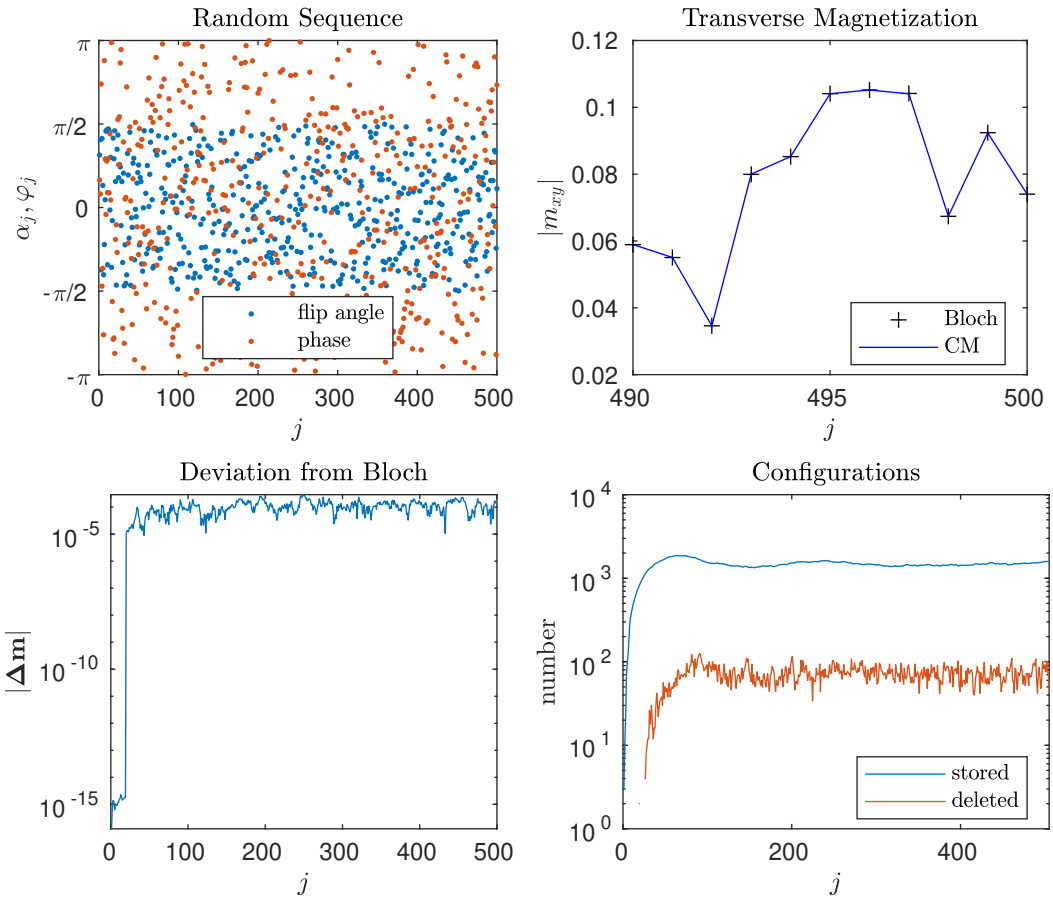

Figure S1: CCM compared to microscopic Bloch simulation for a pure tissue ($T_1/T_2 = 100/10, m_{eq} = 1$). The balanced SSFP sequence ($\boldsymbol{p} \equiv \mathbf{0}$) comprised randomized RF pulses (α_j, φ_j) (**upper left**) and the duration of each of the 500 intervals was randomly selected from 10 equidistant values, bound by the interval $[\,0.8, 1.2\,]$. **upper right**: Signal magnitude during the last 10 time periods. As required, the CCM and Bloch simulations are consistent. **lower left**: Absolute deviation between CCM and Bloch simulations. **lower right**: In the CCM simulations, configuration vectors with $\|\hat{\boldsymbol{m}}\|_2 < 10^{-5}$ were discarded (red) after every time interval. (generated with `cm_vs_bloch.m`)

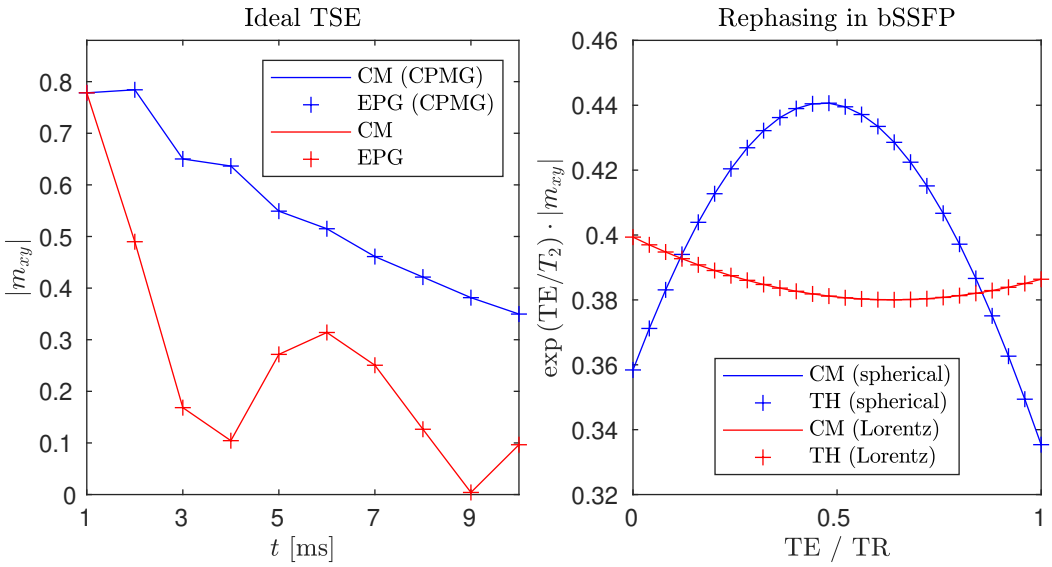

Figure S2: **left**: Comparison between CCM and EPG for an ideal single-shot TSE sequence ($\pm$ CPMG condition) for a pure, static tissue ($T_1/T_2 = 100/10, m_{eq} = 1$) and an echo spacing equal to 1. The relative B_1^+ was set to 0.8 to generate stimulated echoes. (generated with `tse_ideal.m`) **right**: Rephasing of static susceptibility effects in balanced SSFP sequences as a function of TE/TR. The CCM is compared with theory (2) for a spherical and a Lorentzian frequency distribution, showing the known effect (2) that the rephasing is destroyed by the (too) slow decay (in frequency space) of the Lorentzian distribution. Simulation parameters are equivalent to those of Figure 9c in (3). (generated with `bssfp_susc.m`)

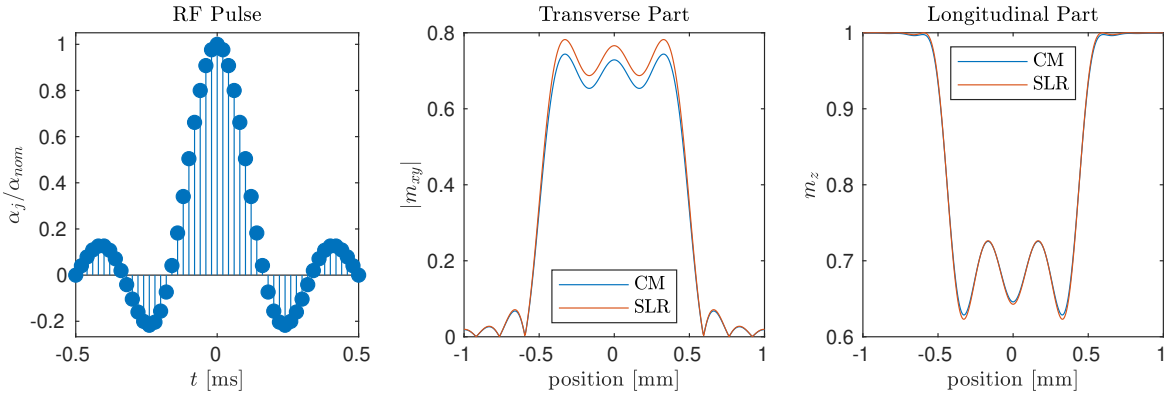

Figure S3: **left**: RF pulse in hard pulse approximation (Sinc pulse of duration 1 ms, slice thickness 1 mm with 50 support points and three zero-crossings on each side. Center slice flip angle = 50°), **middle**: simulated transverse magnetization profile (magnitude) for SLR (5) and CCM after applying the RF pulse to equilibrated longitudinal magnetization ($R_1 = 0, R_2 = 0.1$ ms$^{-1}, D = 0, m_{eq} = 1$), **right**: same for longitudinal component. For $R_2 = 0$, the CCM coincides with SLR, as required. (generated with `selective_excitation.m`)

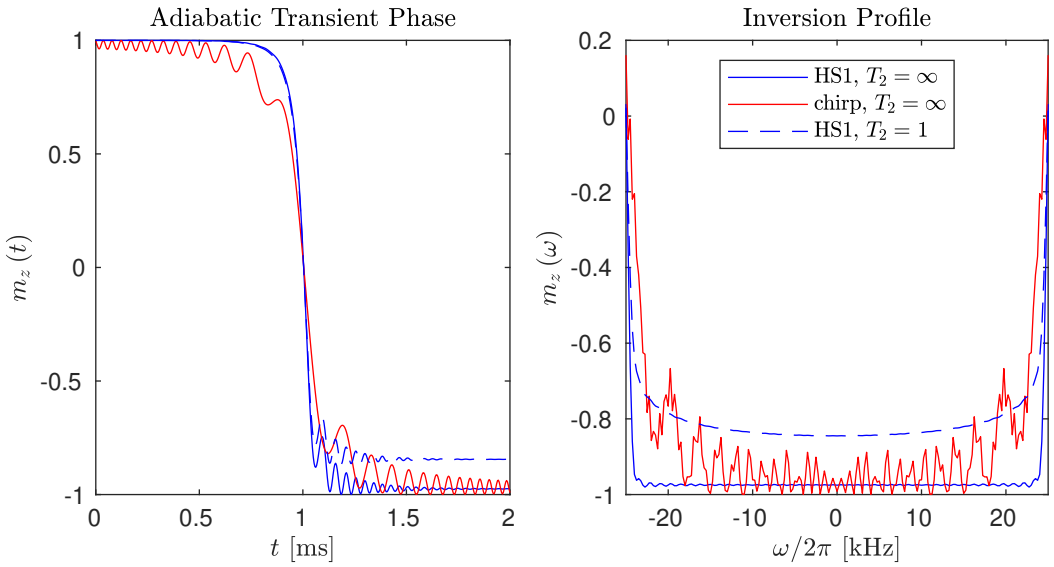

Figure S4: Adiabatic full-passage HS1 and chirp pulse (duration 2 ms, frequency range ± 25 kHz). Specific pulse parameters are listed in Table 1 of ref. (6). The pulse was split into 500 segments in the CCM simulation. When T_2 becomes comparable to the RF pulse duration, we observe incomplete inversion (dashed line). **left**: Evolution of longitudinal magnetization during the RF pulse for spins on resonance ($\omega = 0$). **right**: Longitudinal magnetization as a function of off-resonance frequency ω at the end of the RF pulse. (generated with `adiabatic_pulse.m`)

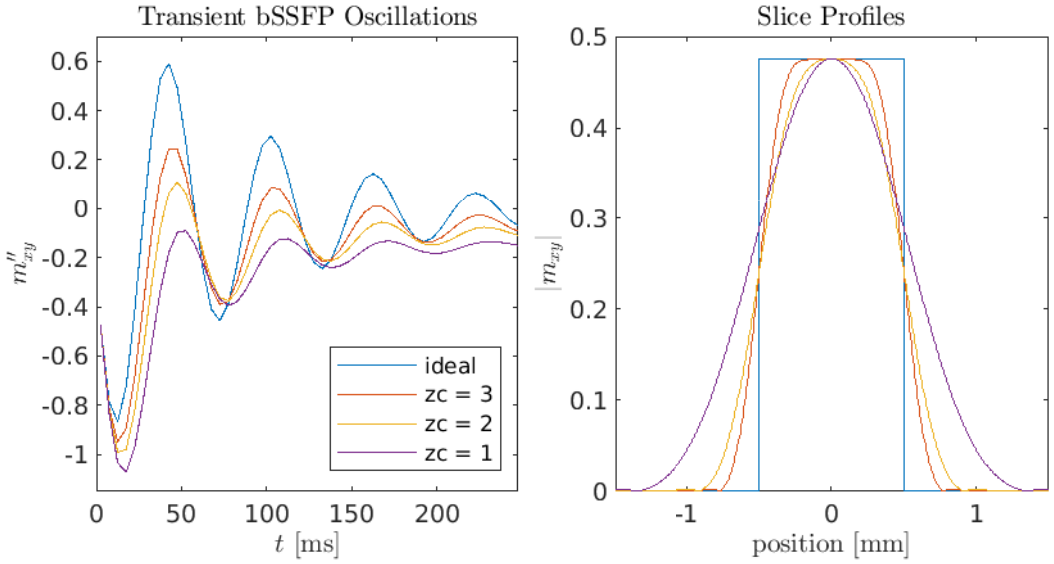

Figure S5: Dependence of transient bSSFP oscillations (**left**) on the quality of the RF slice profile (**right**). The simulation shows Hamming filtered sinc pulses with 50 segments, center slice flip angle = 30° for a variable number of zero crossings (zc) on each side. For comparison, an ideal slice profile was calculated as well (approximately realized as an instantanous RF pulse with constant flip angle). The signals (shown is the imaginary part) were normalized to generate equal initial values (immediately after the first RF pulse). Timing parameters were $T_1/T_2/\mathrm{TR} = 500/50/5$ ms and spins were assumed to be on resonance ($\omega \equiv 0$, corresponding to stop band conditions). (generated with `gre_ideal_vs_real.m`)

2 Bulk Motion

Bulk motion can be added to the CCM without problems. We can define it by a spatio-temporal velocity field $\boldsymbol{v}\,(\boldsymbol{x},t)$, such that tissue, located at position $\boldsymbol{x}_0$ at time $t=0$, can be found[4] at

$$\boldsymbol{x}_t \;:=\; \int_0^t dt'\,\boldsymbol{v}\left(\boldsymbol{x}_{t'},t'\right) \;+\; \boldsymbol{x}_0 \qquad \text{[S1]}$$

at later times $t>0$.

Considering the state $\boldsymbol{s}$, we just have to choose, whether we want to follow tissue motion (tagged volume) or not (fixed location).

Let us look at both options:

2.1 Tagged Volume

We consider a tagged microscopic volume, moving according to Eq. [S1].

The temporal evolution of the ensemble state $\boldsymbol{s}\,(\boldsymbol{x}_0,t)$ *inside*[5] the tagged volume is then governed by

$$\partial_t\,\boldsymbol{s} \;=\; \boldsymbol{X}\,\boldsymbol{s} \;-\; i\left(\,\gamma\,\boldsymbol{G}\,\boldsymbol{x}_0 \;+\; \omega \;+\; \delta\omega\,\right)\boldsymbol{P}\,\boldsymbol{s} \;-\; \boldsymbol{R}\left(\,\boldsymbol{s}-\boldsymbol{s}_{eq}\,\right) \qquad \text{[S2]}$$

which differs from Eq. [3] by an additional term on the RHS, proportional to

$$\delta\omega\,(\boldsymbol{x}_0,t) \;:=\; \omega\,(\boldsymbol{x}_t,t)-\omega\,(\boldsymbol{x}_0) \;+\; \gamma\,\boldsymbol{G}\,(t)\,(\,\boldsymbol{x}_t-\boldsymbol{x}_0\,) \qquad \text{[S3]}$$

and describes the deviation from $\omega\,(\boldsymbol{x}_0)$ due to time-dependent bulk off-resonance and/or bulk motion.

To adapt the CCM [4], we just replace $\boldsymbol{x}$ by the *initial* location $\boldsymbol{x}_0$:

$$\boldsymbol{s}\,(\boldsymbol{x}_0,t) \;=:\; \int d\boldsymbol{p}\,d\tau\,e^{-\,i\,[\,\omega\,(\boldsymbol{x}_0)\,\tau\,+\,\boldsymbol{p}\,\boldsymbol{x_0}\,]}\,\hat{\boldsymbol{s}}\,(\boldsymbol{p},\tau,\boldsymbol{x}_0,t) \qquad \text{[S4]}$$

Inserting the CCM [S4] into [S2] yields

$$\partial_t\,\hat{\boldsymbol{s}} \;=\; \hat{\boldsymbol{X}}\,\hat{\boldsymbol{s}} \;-\; \left(\,\gamma\,\boldsymbol{G}\,\nabla_{\boldsymbol{p}} \;+\; \partial_\tau \;+\; i\,\delta\omega\,\right)\boldsymbol{P}\,\hat{\boldsymbol{s}} \;-\; \boldsymbol{R}\left(\,\hat{\boldsymbol{s}}-\hat{\boldsymbol{s}}_{eq}\,\right) \qquad \text{[S5]}$$

The main benefit of the tagged volume picture is that it is *safe* in the sense that we may rely on a time-invariant tissue composition.

The expression for the recorded signal [13] needs to be adapted though:

$$d_\gamma\,(t) \;=\; \int d\boldsymbol{x}_0\,c_\gamma\,(\boldsymbol{x}_t,t)\;m_+\,(\boldsymbol{x}_0,t) \;+\; \eta_\gamma\,(t) \qquad \text{[S6]}$$

[4] Note that $\boldsymbol{v}$ does *not* include diffusive motion of individual spins.

[5] With respect to spin diffusion, the microscopic volume must be regarded as open.

The explicit solutions (and numerical implementation (1)) for diffusion (Bloch-Torrey) and magnetization exchange/transfer (Bloch-McConnell), derived below, include bulk motion in the tagged volume picture.

2.2 Fixed Location

Here, we simply look at the temporal evolution of the spin state at some *fixed* location $\boldsymbol{x}$.

To describe this situation, we need to insert a flow term into Eq. [3]

$$\partial_t \boldsymbol{s} \;=\; \boldsymbol{X}\,\boldsymbol{s} \;-\; i\,\big(\,\gamma\,\boldsymbol{G}\,\boldsymbol{x} \;+\; \omega\,\big)\,\boldsymbol{P}\,\boldsymbol{s} \;-\; \boldsymbol{v}\,\nabla_{\boldsymbol{x}}\,\boldsymbol{s} \;-\; \boldsymbol{R}\,\big(\,\boldsymbol{s} - \boldsymbol{s}_{eq}\,\big) \qquad \text{[S7]}$$

and leave the CCM [4] untouched.

The differential equation in configuration space then approximately becomes

$$\partial_t\,\hat{\boldsymbol{s}} \;\approx\; \hat{\boldsymbol{X}}\,\hat{\boldsymbol{s}} \;-\; \big(\,\gamma\,\boldsymbol{G}\,\nabla_{\boldsymbol{p}} \;+\; \partial_\tau\,\big)\,\boldsymbol{P}\,\hat{\boldsymbol{s}} \;+\; i\,(\boldsymbol{v}\boldsymbol{p})\,\hat{\boldsymbol{s}} \;-\; \boldsymbol{R}\,\big(\,\hat{\boldsymbol{s}} - \hat{\boldsymbol{s}}_{eq}\,\big) \qquad \text{[S8]}$$

if we ignore spatial derivatives with respect to bulk off-resonance and tissue composition.

While this approach does not require any further changes, it is not safe in the aforementioned sense.

2.3 Motion along Unbalanced Gradients

We consider a periodic ($\tilde{\tau}$), unbalanced ($\tilde{\boldsymbol{p}}$) SSFP sequence with instantaneous RF pulses in presence of bulk motion with constant velocity: $\boldsymbol{x}_t = \boldsymbol{x}_0 + \boldsymbol{v}\,t$. Ignoring possible time-dependent off-resonance effects and possibly variable higher order gradient moments (e.g. due to phase encoding), the motion-induced sweep of the off-resonance frequency [S3] in a tagged volume can be written in the form

$$\delta\omega\,(j\,\tilde{\tau}) \;=\; -\,j\,\tilde{\boldsymbol{p}}\,\boldsymbol{v} \;+\; c \qquad \text{[S9]}$$

where c is some constant, which does not depend on j. Under these conditions, bulk motion becomes equivalent to RF spoiling (8) with a phase difference increment $\phi = \tilde{\tau}\,\tilde{\boldsymbol{p}}\,\boldsymbol{v}$. Figure S6 (right) confirms this by establishing the equality between the CCM simulation in presence of constant motion and the corresponding RF spoiled steady-state. It also demonstrates the known effect that tissues with larger T_2 values are more affected by signal loss due to motion (9).

3 Diffusion

3.1 Bloch-Torrey Equations

The Bloch-Torrey equations (10) add diffusion effects to the Bloch equations. As for the Bloch equations, we may identify the state $\boldsymbol{s}$ with the complex magnetization density $\boldsymbol{m}$ in Eq. [2] and write the Bloch-Torrey equations in the form [S2], if we set

$$\boldsymbol{X} \;:=\; -\,i\,\boldsymbol{\Omega}_1 \;-\; i\,\delta\omega_*\,\boldsymbol{P} \;+\; \nabla_{\boldsymbol{x}_0}\,\boldsymbol{D}\,\nabla_{\boldsymbol{x}_0} \qquad \text{[S10]}$$

The individual terms on the RHS are defined as follows:

- The matrix $\boldsymbol{\Omega}_1\,(\boldsymbol{x}_t, t)$ generates a rotation due to RF pulses.
- $\delta\omega_* \;:=\; -\,\sigma\,\omega_{\mathrm{rf}}$ is the frequency offset due to chemical shift σ in the phase-modulated frame, rotating with the RF carrier frequency ω_{rf}.
- The matrix $\boldsymbol{P} := \mathrm{diag}\,[\,1, -1, 0\,]$ describes the opposed direction of precession for the two complex conjugate transverse components.
- $\boldsymbol{D}\,(\boldsymbol{x}_0)$ denotes the diffusion tensor[6].

Relaxation matrix $\boldsymbol{R}\,(\boldsymbol{x}_0)$ and proton density $\boldsymbol{s}_{eq}\,(\boldsymbol{x}_0) = \boldsymbol{m}_{eq}\,(\boldsymbol{x}_0)$ in Eq. [S2] are defined as for the Bloch equations in the main text (cf. Methods section, therein).

The generalization to composite tissues is trivial for non-interacting subspecies and can be handled by independent solution and subsequent addition.

As shown above, the corresponding differential equation for the configuration $\hat{\boldsymbol{m}}$ is given by Eq. [S5] and the definition

$$\hat{\boldsymbol{X}} \;\approx\; -\,i\,\boldsymbol{\Omega}_1 \;-\; i\,\delta\omega_*\,\boldsymbol{P} \;-\; \boldsymbol{p}^T\boldsymbol{D}\,\boldsymbol{p}\cdot\boldsymbol{I}_3 \qquad \text{[S11]}$$

$\boldsymbol{I}_3$ denotes the 3×3 unit matrix.

In the diffusion term we only considered spatial derivatives related to applied gradients and the $\boldsymbol{p}$-dependence reflects the fact that short range modulations of the magnetization density are more susceptible to diffusion damping.

3.2 Recurrence Relations

For a time interval $I := [\,t_a, t_b\,]$ without RF pulses ($\boldsymbol{\Omega}_1 \equiv \boldsymbol{0}$), the differential equations [S5] can be integrated and we obtain recurrence relations for the transverse and longitudinal components

$$\begin{aligned}\hat{m}_{\pm}\,(\boldsymbol{p}, \tau, t) \;&=\; e^{\mp\,i\,\int_{t_a}^{t} dt'\,\delta\omega(t')}\,e^{-\,(R_2\,\pm\,i\,\delta\omega_*)\,\delta t}\,e^{-\,\int_{t_a}^{t} dt'\,(\boldsymbol{p}\,\mp\,\boldsymbol{p}_{t'})^T\boldsymbol{D}\,(\boldsymbol{p}\,\mp\,\boldsymbol{p}_{t'})} \\ &\quad\cdot\;\hat{m}_{\pm}\,(\,\boldsymbol{p}\mp\delta\boldsymbol{p},\;\tau\mp\delta t,\;t_a)\end{aligned} \qquad \text{[S12]}$$

$$\hat{m}_z\,(\boldsymbol{p}, \tau, t) \;=\; e^{-\,\left(R_1\,+\,\boldsymbol{p}^T\boldsymbol{D}\,\boldsymbol{p}\right)\delta t}\,\hat{m}_z\,(\boldsymbol{p},\;\tau,\;t_a) \;+\; \left(\,1 - e^{-\,R_1\,\delta t}\,\right)\hat{m}_{eq,z}\,(\boldsymbol{p}, \tau) \qquad \text{[S13]}$$

[6] Despite invariant tissue composition of the tagged volume, the diffusion tensor can still depend on time due to bulk motion (deformation, reorientation). We ignore such effects.

for any $t \in I$. For better readability, we dropped the argument $\boldsymbol{x}_0$ and defined[7]

$$\boldsymbol{p}_{t'} \;:=\; \gamma \int_{t'}^{t} dt'' \, \boldsymbol{G}\left(t''\right) \qquad \text{[S14]}$$

3.3 Diffusion Damping in SSFP

We now consider an ideal SSFP sequence, consisting of identical RF pulses, separated by time intervals of constant duration $\tilde{\tau}$ and zero-order gradient moment $\tilde{\boldsymbol{p}}$. We assume isotropic diffusion ($\boldsymbol{D} = D \cdot \boldsymbol{I}_3$) and a constant gradient ($\boldsymbol{G}\left(t\right) \equiv \boldsymbol{G}$) in each time interval. The diffusion related damping factor then becomes

$$e^{-\,\tilde{\tau} D \left[\, p^2 \,\mp\, \boldsymbol{p}\tilde{\boldsymbol{p}} \,+\, \tilde{p}^2/3 \,\right]} \qquad \text{[S15]}$$

for the transverse components [S12] and $e^{-\,\tilde{\tau} D\, p^2}$ for the longitudinal component [S13], in accordance[8] with Kaiser et al. (11). Figure S6 (left) demonstrates numerical agreement with an exact analytical solution (12).

4 Magnetization Exchange (ME) and Transfer (MT)

4.1 Bloch-McConnell Equations

The Bloch-McConnell equations (13) describe magnetization exchange (ME) and transfer (MT) between a set of q coupled subspecies. The state $\boldsymbol{s}$ is defined by the corresponding set of q magnetization densities $\boldsymbol{m}_\alpha$ (each defined according to the convention [2]), which can be arranged in a stacked vector

$$\boldsymbol{s} \;:=\; \begin{bmatrix} \boldsymbol{m}_+ \\ \boldsymbol{m}_- \\ \boldsymbol{m}_z \end{bmatrix} \qquad \text{[S16]}$$

such that $\left[\, \boldsymbol{m}_\pm \,\right]_\alpha := \left[\, \boldsymbol{m}_\alpha \,\right]_\pm$ and $\left[\, \boldsymbol{m}_z \,\right]_\alpha := \left[\, \boldsymbol{m}_\alpha \,\right]_z$.

In this convention, the matrix $\boldsymbol{X}$ in Eq. [S2] can be written as

$$\boldsymbol{X} \;:=\; -\,i\,\boldsymbol{\Omega}_1 \;-\; i\,\boldsymbol{P} \otimes \delta\boldsymbol{\omega}_* \;+\; \boldsymbol{I}_3 \otimes \boldsymbol{K} \qquad \text{[S17]}$$

'$\otimes$' denotes the Kronecker product and the individual terms on the RHS are defined as follows:

[7] δt and $\delta \boldsymbol{p}$ are defined as in Eq. [8].

[8] The linear term $\propto \boldsymbol{p}$ appears with opposite sign, compared with Eq. 18 in (11). This is only due a different definition of $\boldsymbol{p}$, which refers to the starting value at t_a in (11), whereas it denotes the final value at time point t in Eq. [S12]. (The latter convention is more convenient to verify that [S12] solves the differential equation [S5].)

- The matrix $\boldsymbol{\Omega}_1$ is composed of submatrices $\boldsymbol{\Omega}_{1\alpha}$, each of which either rotates or saturates (14–16) subspecies α.
- The precession matrix $\boldsymbol{P}$ is defined as in the Bloch(-Torrey) equations.
- The elements of the diagonal matrix $\delta\boldsymbol{\omega}_*$ contain the frequency offset due to chemical shift σ_α for each subspecies α and are therefore defined by $[\,\delta\boldsymbol{\omega}_*\,]_{\alpha\alpha} := -\,\sigma_\alpha\,\omega_{\mathrm{rf}}$.
- The $q \times q$ matrix $\boldsymbol{K}$ comprises the transition rates between subspecies. For $\alpha \neq \beta$, the rate $k_{\alpha\beta}$ corresponds to the transition $\beta \to \alpha$. The matrix $\boldsymbol{K}$ must satisfy two sum rules, related to particle conservation and long time behavior

$$k_{\alpha\alpha} \;=\; -\sum_{\beta\neq\alpha} k_{\beta\alpha} \qquad \text{and} \qquad \sum_{\beta} k_{\alpha\beta}\cdot m_{eq\,\beta} \;=\; 0 \qquad \text{for all } \alpha. \tag{S18}$$

The terms $\boldsymbol{R}$ (relaxation/repolarization) and $\boldsymbol{s}_{eq}$ (thermal equilibrium) in Eq. [S2] differ from the Bloch(-Torrey) equations:

- With $[\,\boldsymbol{R}_j\,]_{\alpha\beta} := \delta_{\alpha\beta}\cdot R_{j\alpha}$ for $j \in \{1,2\}$, the diagonal relaxation matrix $\boldsymbol{R}$ reads

$$\boldsymbol{R} \;:=\; \begin{bmatrix} \boldsymbol{R}_2 & & \\ & \boldsymbol{R}_2 & \\ & & \boldsymbol{R}_1 \end{bmatrix} \tag{S19}$$

- $\boldsymbol{s}_{eq}$ collects the proton densities of each component. In the convention [S16] we get

$$\boldsymbol{s}_{eq} \;:=\; \begin{bmatrix} \boldsymbol{0} \\ \boldsymbol{0} \\ \boldsymbol{m}_{eq} \end{bmatrix} \tag{S20}$$

The matrix $\hat{\boldsymbol{X}}$ in the differential equation [S5] is identical to $\boldsymbol{X}$.

4.2 Recurrence Relations

As before, the evolution during an interval without RF pulses leads to closed form recurrence relations for the transverse and longitudinal components

$$\hat{\boldsymbol{m}}_{\pm}\,(\boldsymbol{p},\tau,t) \;=\; e^{\mp i\,\int_{t_a}^{t} dt'\,\delta\omega(t')}\; e^{\delta t\,(\boldsymbol{K}\,-\,\boldsymbol{R}_2\,\mp\, i\,\delta\boldsymbol{\omega}_*)}\;\hat{\boldsymbol{m}}_{\pm}\,(\,\boldsymbol{p}\mp\delta\boldsymbol{p},\;\tau\mp\delta t,\;t_a) \tag{S21}$$

$$\begin{aligned}\hat{\boldsymbol{m}}_{z}\,(\boldsymbol{p},\tau,t) \;=\;& e^{\delta t\,(\boldsymbol{K}\,-\,\boldsymbol{R}_1)}\;\hat{\boldsymbol{m}}_{z}\,(\boldsymbol{p},\;\tau,\;t_a) \\ &-\;(\boldsymbol{K}\;-\;\boldsymbol{R}_1)^{-1}\,\big(\,\boldsymbol{I}_q - e^{\delta t\,(\boldsymbol{K}\,-\,\boldsymbol{R}_1)}\,\big)\,\boldsymbol{R}_1\,\hat{\boldsymbol{m}}_{eq,z}\,(\boldsymbol{p},\tau)\end{aligned} \tag{S22}$$

(Since $\boldsymbol{K}$ does not commute with $\boldsymbol{R}_j$ and $\delta\boldsymbol{\omega}_*$, the exponentials cannot not be factorized (17).)

4.3 Comparison with EPG-X (17)

Figure S7 shows that the CCM agrees with EPG-X by Malik et al. (17) and exact closed form solutions (14, 18) of the steady-state of balanced and spoiled SSFP sequences for two compartments in ME and MT.

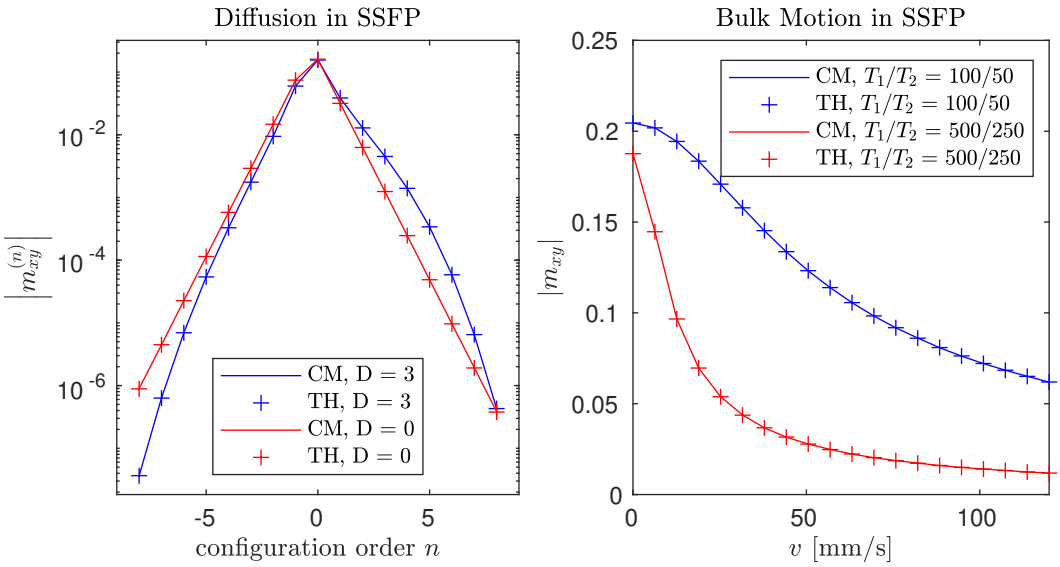

Figure S6: **left**: Diffusion sensitivity of steady-state unbalanced SSFP (flip angle = 30°, $\tilde{\tau} = 5\,\text{ms}$, $\tilde{p} = 0.05\,\mu\text{m}^{-1}$) for a pure tissue ($T_1/T_2 = 500/50$ ms, $D = 3\,\mu\text{m}^2\text{ms}^{-1}$), compared with absence of diffusion. Full agreement with exact theory (TH) according to Freed et al. (12) could be obtained for all configurations (labeled by configuration order n). (generated with `diff_ssfp.m`) **right**: Signal decay in unbalanced SSFP (flip angle = 90°, $\tilde{\tau} = 5$, $\tilde{p} = 2\pi\,\text{mm}^{-1}$) in presence of constant tissue motion (v) along the crusher gradient. (generated with `motion_ssfp.m`, TH calculated with analytical solution from (9))

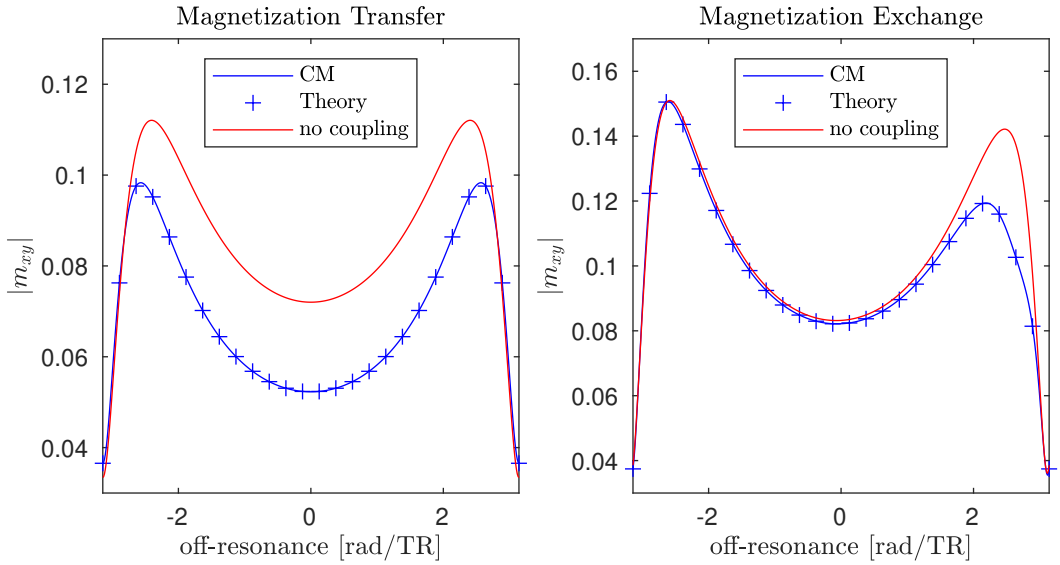

Figure S7: Balanced SSFP (TR = 5 ms, $\alpha = 10°$) signal amplitude as a function of off-resonance for two coupled compartments in presence of magnetization transfer (left) and exchange (right), both compared with their respective uncoupled counterparts (red). In both cases, the CCM agrees perfectly with the available analytical solution. Tissue parameters were taken from Table 1 in ref. (17) and the calculations correspond to Figure 3 therein: **left**: White matter MT model, equivalent to Figure 3 (a,b) of ref. (17). **right**: Myelin water exchange model with nonzero chemical shift ($\delta_b = 0.1$ ppm), equivalent to Figure 3 (d) of ref. (17). (generated with `ME_MT_ssfp.m`)

5 Quantum Mechanical Models

5.1 Master Equation

The CCM also applies to cases, which require a quantum mechanical treatment (like J-coupling) and is not limited to spin-$\frac{1}{2}$ systems. This simply follows from the fact that the master equation, which governs the evolution of composite density matrices (19), is compatible with Eq. [3]. The state vector $\boldsymbol{s}$ then contains the matrix elements of the density matrix and the linear operator $\boldsymbol{L}$ corresponds to a suitably defined trace. The nonzero elements of the diagonal precession term $\boldsymbol{P}$ depend on the quantum numbers and are not necessarily restricted to the set $\{0, \pm 1\}$. To provide an illustrative example, we briefly discuss the connection to the SLR forward transform (5):

5.2 Connection to SLR Forward Transform

The spin state is defined by a 2×2 density matrix $\boldsymbol{\sigma}$ such that the 4×1 state vector $\boldsymbol{s}$ can be obtained by stacking its columns. This just leads to the superoperator formalim (20), in which the evolution of $\boldsymbol{s}$ is determined by a quantum mechanical master equation of the form [3].

The SLR algorithm (5) decomposes RF pulses according to the hard pulse approximation into an alternating series of instantaneous small angle rotations, separated by intervals of free precession in presence of gradients. In the CCM, the rotations are described by 4×4 unitary matrices $\boldsymbol{U}_j$, cf. Eq. [7] and we set $\boldsymbol{X} = \boldsymbol{0}$ in the free precession intervals. Ignoring relaxation ($\boldsymbol{R} = \boldsymbol{0}$), we only need to specify the matrix $\boldsymbol{P}$ in the differential Eq. [3], which takes the form

$$\boldsymbol{P} := \begin{bmatrix} 0 & & & \\ & 1 & & \\ & & -1 & \\ & & & 0 \end{bmatrix} \qquad \text{[S23]}$$

With these expressions, it is not difficult to integrate the differential equation [5] for the free precession in closed form. The iterated recurrence relations, which generate the configurations $\hat{\boldsymbol{s}}^{(n)}$ in the CCM [4] (= slice profile) from the RF pulse shape then just reproduce[9] the SLR forward transform.

To extract the final slice profile, we apply the operator $\boldsymbol{L}$ to the CCM [4]. After evaluating the associated traces, we get[10]

$$\boldsymbol{L} = \begin{bmatrix} L_+ \\ L_- \\ L_z \end{bmatrix} := \begin{bmatrix} 0 & 1 & 0 & 0 \\ 0 & 0 & 1 & 0 \\ \frac{1}{2} & 0 & 0 & -\frac{1}{2} \end{bmatrix} \qquad \text{[S24]}$$

[9] Just like in SLR, one can exploit symmetries to simplify the problem.

[10] We assume the proton density to be included in the definition of the state $\boldsymbol{s}$.

References

1. Ganter C. Configuration Model Toolkit (CoMoTk) 2021;doi:10.5281/zenodo.5347194.
2. Ganter C. Static susceptibility effects in balanced SSFP sequences. Magn Reson Med 2006; 56:687–691. doi:10.1002/mrm.20986.
3. Leupold J. Steady-state free precession signals of arbitrary dephasing order and their sensitivity to T2*. Concepts in Magnetic Resonance Part A 2017;p. e21435.
4. Scheffler K, Hennig J. Is TrueFISP a gradient-echo or a spin-echo sequence? Magnetic Resonance in Medicine 2003;pp. 395–397.
5. Pauly J, Le Roux P, Nishimura D, Macovski A. Parameter relations for the Shinnar-Le Roux selective excitation pulse design algorithm (NMR imaging). IEEE Trans Med Imaging 1991;10:53–65. doi:10.1109/42.75611.
6. Garwood M, DelaBarre L. The return of the frequency sweep: designing adiabatic pulses for contemporary NMR. Journal of magnetic resonance 2001;153:155–177.
7. Ganter C, Settles M, Dregely I, Santini F, Scheffler K, Bieri O. B1+-mapping with the transient phase of unbalanced steady-state free precession. Magn Reson Med 2013;70:1515–1523. doi:10.1002/mrm.24598.
8. Zur Y, Wood ML, Neuringer LJ. Spoiling of transverse magnetization in steady-state sequences. Magnetic Resonance in Medicine 1991;pp. 251–263.
9. Ganter C. Steady state of gradient echo sequences with radiofrequency phase cycling: Analytical solution, contrast enhancement with partial spoiling. Magnetic Resonance in Medicine 2006;pp. 98–107.
10. Torrey HC. Bloch equations with diffusion terms. Phys Rev 1956;104:563–565. doi:10.1103/physrev.104.563.
11. Kaiser R, Bartholdi E, Ernst RR. Diffusion and field-gradient effects in NMR Fourier spectroscopy. The Journal of Chemical Physics 1974;60:2966–2979. doi:10.1063/1.1681477.
12. Freed DE, Scheven UM, Zielinski LJ, Sen PN, Hürlimann MD. Steady-state free precession experiments and exact treatment of diffusion in a uniform gradient. The Journal of Chemical Physics 2001;115:4249–4258. doi:10.1063/1.1389859.
13. McConnell HM. Reaction rates by nuclear magnetic resonance. The Journal of Chemical Physics 1958;28:430–431. doi:10.1063/1.1744152.
14. Gloor M, Scheffler K, Bieri O. Quantitative magnetization transfer imaging using balanced SSFP. Magnetic Resonance in Medicine 2008;pp. 691–700.
15. Graham SJ, Henkelman RM. Understanding pulsed magnetization transfer. Journal of Magnetic Resonance Imaging 1997;pp. 903–912.
16. Bloembergen N, Purcell EM, Pound RV. Relaxation effects in nuclear magnetic resonance absorption. Physical Review 1948;pp. 679–712.
17. Malik SJ, Teixeira RPA, Hajnal JV. Extended phase graph formalism for systems with magnetization transfer and exchange. Magn Reson Med 2017;80:767–779. doi:10.1002/mrm.27040.

18. Deoni SCL, Rutt BK, Arun T, Pierpaoli C, Jones DK. Gleaning multicomponent T1 and T2 information from steady-state imaging data. Magnetic Resonance in Medicine 2008;pp. 1372–1387.

19. Binsch G. Unified theory of exchange effects on nuclear magnetic resonance line shapes. Journal of the American Chemical Society 1969;pp. 1304–1309.

20. Richard R Ernst AW Geoffrey Bodenhausen. Nuclear Magnetic Resonance. Royal Society of Chemistry, 1986. ISBN 9780851863825. doi:10.1039/9781847553713.